Underground Injection Control – Class VI Permit Application for Mockingbird Carbon Storage Project Injection Wells No. 01, No. 02, No. 03, and No. 04

SECTION 2 – PLUME MODEL

Mockingbird Carbon Storage Project
Allen Parish, Louisiana
ExxonMobil Low Carbon Solutions Onshore Storage, LLC
March 2025

SECTION 2 – PLUME MODEL

TABLE OF CONTENTS

Figures

[redacted]

[redacted]

Tables

[redacted]

2.1 Introduction

[redacted] of the Louisiana Administrative Code, Title 43 (LAC43): XVII **§3615.B.2**.

[redacted]

[redacted]

2.2 Objectives

[redacted] LAC43: XVII **§3615.B.2**:

- [redacted] (LAC43: XVII **§3615.B.3**).
- [redacted] (LAC43: XVII **§3615.C.1**) [redacted]

[redacted] [redacted]

[redacted] [redacted]

- [redacted] (LAC43: XVII **§3615.C.3**).
- [redacted] (LAC43: XVII **§3615.C.2**).
- [redacted] (LAC43: XVII **§3615.C.4**).

2.3 Modeling and Simulation Framework

2.3.1 Software

2.3.1.1 Petrel™ Software Suite

The SLB Petrel software suite (ver. 2023.6) was chosen to create a detailed geologic model for the CS site. This state-of-the-art software is used worldwide and provides a platform to integrate subsurface data—including well logs, cores, and seismic data—to build a reliable representation of the subsurface reservoir. The Petrel-developed geologic model incorporates the different geologic layers of the site, including the upper confining zone (UCZ, upper seal), [redacted] Using Petrel, the porosity and permeability properties of the reservoirs were distributed using industry-standard geostatistical methods, incorporating all subsurface characterization results. This integrated subsurface characterization and geologic modeling workflow ensures a more precise depiction of the reservoir in the model.

2.3.1.2 Carbon Storage Simulation Using Intersect Suite

A reservoir simulation platform is required to predict CO_2 migration and reservoir pressure change. For the Mockingbird Project, SLB's Intersect™ (ver. 2023.4) is used, with the geologic model developed in Petrel as input. Intersect is a widely recognized petroleum-engineering simulation tool. The simulator enables the user to define an initial reservoir condition in terms of the pressure, saturation, and composition of fluid phase, and to advance this solution forward in time. This modeling is achieved by solving mathematical equations that express the fact that mass is conserved in the reservoir and that the fluid phases are in thermodynamic equilibrium.

Specific functionalities have been developed in Intersect for carbon storage modeling, including CO_2 solubility in brine by using the Component Solubility in Water (CSIW) module. The software can handle large data sets and multiple grids, and offers various tools for data management, visualization, and uncertainty analysis.

2.3.2 Data Sources

The data sources used to build the geologic and dynamic model include 3D and 2D seismic data, offset well logs, core data, and publicly available literature.

Public databases and literature were initially reviewed at both regional and site-specific levels. The regional review identified the major trends in the project area and the surrounding region. These trends were compared to more site-specific data to provide a higher confidence in the reservoir properties. [redacted]. These input parameters are discussed in *Section 2.6.*

Offset well log analysis was conducted to characterize the reservoir and populate the geologic model. Openhole log data includes gamma ray (GR), spontaneous potential (SP), resistivity, porosity (sonic, neutron, density), photoelectric factor, caliper, and other related analyses. These well logs helped determine formation tops, rock properties, and temperature gradients. For facies modeling, 216 wells with shale volume (Vshale) logs were used. Petrophysical analysis was performed on 20 wells in the project vicinity to characterize the target injection zone and subsequent confining layers.

Three-dimensional seismic data was used in conjunction with formation tops identified through log analysis to enhance the characterization of the reservoir and to identify major structural horizons as shown in *Appendix B2* (*Section 1 – Site Characterization*). The 3D seismic data also allows for greater clarity of the subsurface, such as faults, salt domes, or any other structural features. This data enhanced the accuracy of the geologic model by providing a clearer understanding of the targeted stratigraphy. Modern core data and well data from the nearby stratigraphic test well [redacted] was used to determine the porosity-permeability relationship in the [redacted] formations.

Additional data will be collected during the drilling of wells for the proposed project. A detailed description of the Pre-Operational Testing Plan is outlined in *Section 4 – Well Construction Plan and Operating Conditions*.

2.4 CO_2 Trapping Mechanisms

In a CS project, four primary trapping mechanisms sequester the supercritical CO_2, schematically represented in Figure 2-1. In the following sections, all four mechanisms— (1) structural and stratigraphic trapping, (2) residual trapping, (3) solubility trapping, and (4) mineral trapping—are discussed, along with how the simulation software captures these mechanisms. The mineral trapping mechanism is not explicitly included in the current CS modeling process. This mechanism is excluded because, although it is widely considered as a valid and important trapping mechanism, the speed and extent of its occurrence are still being studied—but are generally expected to occur over long periods of time. Omitting this trapping mechanism leads to a conservative forecast for the CO_2 migration footprint.

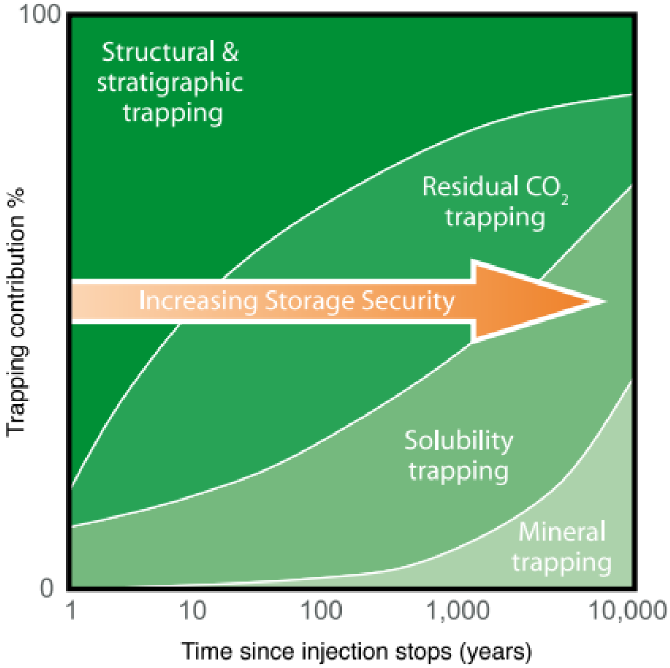

Figure 2-1 – CO_2 Storage Mechanisms (Metz et al., 2005)

2.4.1 Structural and Stratigraphic Trapping

Structural trapping is a physical form of trapping where injected CO_2 is immobilized by the presence of sealing faults, pinchouts, or other forms of geologic traps. Like naturally occurring hydrocarbon reservoirs, CO_2 can be stored in anticlinal folds. Supercritical CO_2 is a low-viscosity fluid, less dense than the surrounding brine found in the injection zone. The CO_2 will continue to rise until its buoyant forces are no longer greater than the capillary entry pressure of the caprock. [redacted]

In the current study, equation of state (EOS) calculations are performed to determine the phase of CO_2. These formulae can predict the density of the injected fluid at any location based on pressure and temperature. Intersect's compositional fluid modeling adopts the Redlich-Kwong-Soave-Peng-Robinson family of EOS in cubic form, which has long been the industry standard in compositional reservoir simulation. The method implemented here is Peng-Robinson.

2.4.2 Residual Gas Trapping

Residual gas or capillary trapping is a form of physical trapping. During active injection, viscous forces drive CO_2 into brine-filled pore space, displacing water. When the CO_2 front moves, the trailing end of the CO_2-filled pore space undergoes hysteresis and water displaces CO_2. Depending on CO_2 saturation and capillary force, some CO_2 will remain residually trapped within the pore space. This process usually becomes the primary trapping mechanism for saline aquifer carbon storage.

Hysteresis modeling is used in the model to accurately predict the amount of residually trapped supercritical CO_2. Important parameters include trapped gas saturation and relative permeability hysteresis paths, which will be discussed further in *Section 2.6.3*.

2.4.3 Solubility Trapping

Solubility trapping is a form of physical trapping between supercritical CO_2 and brine. Injected CO_2 is soluble in the aqueous phase, and its solubility depends on temperature, pressure, and the aqueous phase salinity. Spycher and Pruess (Intersect Technical Description) have developed a method to calculate the mutual solubility of CO_2 and H_2O for pressures up to 600 bar and temperatures ranging from 12°C to 300°C, accounting for brine salinity. The dynamic simulation software adopted for the Mockingbird Project (i.e., Intersect) implements this method using the CSIW module.

The module allows modeling of three phases: liquid (which typically refers to the liquid phase of hydrocarbon and other components but not water), vapor, and aqueous. In this saline aquifer CO_2 storage project, a hydrocarbon liquid phase does not exist. Two minor limitations exist for this module. First, water does not dissolve in the vapor phase in this approach; therefore, near-wellbore vaporization of water cannot be modeled in the CSIW. This solubility is extremely small and will not impact project evaluation. Second, while the hydrocarbon liquid phase can contain multiple components (including CO_2), only one component can dissolve in water. This limitation does not impact this study, as it focuses exclusively on brine-CO_2 systems.

The vapor component densities and fugacities are calculated using cubic EOS. The viscosities are handled using the Lorenz-Bray-Clark model. The composition of CO_2 in the aqueous phase is calculated using the solubility table provided in the model; the aqueous phase density and viscosity are also provided by the user in the solubility table. Salt is not modeled explicitly, therefore the brine properties are provided as a part of the solubility table.

2.4.4 Mineral Trapping

Mineral or geochemical trapping is a form of chemical trapping that occurs due to reactions between CO_2 and the geochemistry of the formation. During injection of CO_2 into the reservoir, four components interact with each other: (1) CO_2 in the supercritical phase, (2) in situ connate brine, (3) dissolved CO_2 in the aqueous phase, and (4) the formation rock. These interactions can result in mineral precipitation. This new mineral is typically calcium carbonate ($CaCO_3$, i.e., limestone). Mineral trapping can also occur due to the adsorption of CO_2 onto clay minerals.

While geochemical trapping can have a greater impact on CO_2 over hundreds or thousands of years, the short-term effects of these trapping mechanisms are small, and fluid movement is dominated by hydrodynamic and solubility trapping. Geochemical trapping mechanisms were not assumed in the current model.

[redacted]

[redacted]

[redacted]

2.5 3D Geologic Model

Characterization of the [redacted] was carried out to develop an understanding of the sealing effects of the confining zone and characterize the reservoir heterogeneity within the injection zone. Based on the analysis and understanding of the Mockingbird Project area, a 3D geologic model was developed to estimate CO_2 storage potential and evaluate its confinement, both laterally and vertically.

2.5.1 Geologic Model of the AOR

Using available data, an integrated geologic model was developed for the site to represent the structural setting and depositional environment and distribute petrophysical properties within the model boundaries. This model provides a 3D grid to enable predictive CO_2 plume and pressure modeling over time. Available site data used to inform the 3D geologic model includes seismic surveys and legacy well logs, such as SP (original log for Vshale, used in most of the Vshale calculations), GR logs (another lithologic log that can also be used to calculate Vshale, used sparingly in this geologic model), resistivity, bulk density (density porosity), and sonic logs (sonic porosity). The geologic model incorporates regional core, log, and seismic data to characterize structural configuration, net sand, facies and property distribution, and porosity-permeability relationships.

Log properties were upscaled to model resolution and populated in a 3D grid over an area that exceeds the spatial limit of the AOR. The geological model is built with a lateral resolution of 650 feet x 650 feet oriented in a north-south direction, and an average vertical resolution of 5 feet. The total cell count is approximately 22.2 million cells. The geologic model area of interest (AOI, presented in Figure 2-4) covers 199,000 acres (311 square miles) and extends well beyond the predicted plume or AOR boundaries to negate any potential for model-edge effects. The overall workflow adopted for geologic modeling is shown in Figure 2-3.

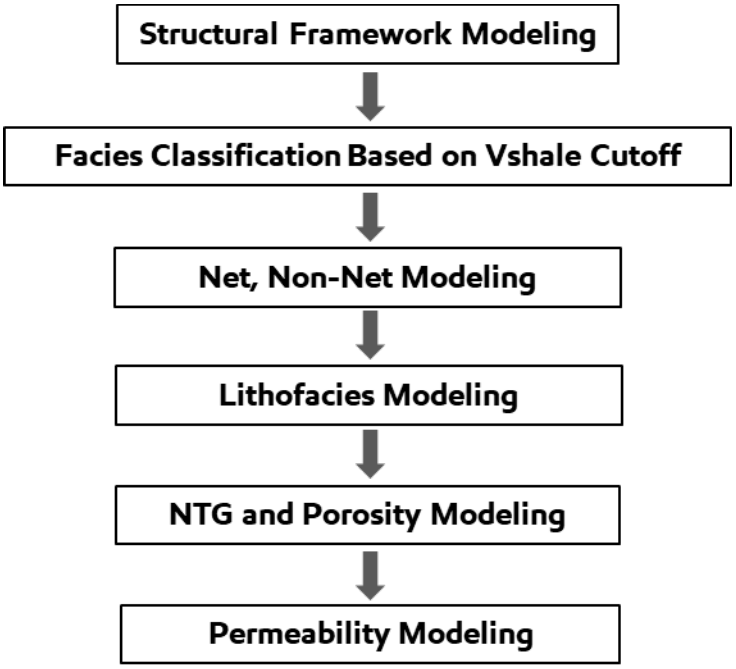

Figure 2-3 – Geologic Modeling Workflow

The model will be updated periodically throughout the life of the project as additional data is collected.

2.5.2 Structural Model

Seismic interpretation was carried out using 3D seismic data that covers 70% of the model AOI and 75% of the AOR. Multiple 2D seismic lines were interpreted to cover the other 30% of the AOI (Figure 2-4). [redacted] detailed in *Section 1.5.2*. [redacted] The well data suitable to assign interpreted formation tops were used to tie the seismic data for formation depths. Layers within the zones were modeled using the stratigraphic layering method.

The structural model captures the throw relationships that were interpreted in the seismic data. Flow and pressure communication across these faults is dictated by the juxtaposition of sands and shales on either side of each fault (sand-on-sand allows flow, sand-on-shale acts as a barrier). Although the structure framework has included two reservoirs above the UCZ—the Middle Fleming and Upper Fleming reservoirs and the corresponding shale layers—this report will focus on the formations below the UCZ.

[redacted]

[redacted]

Figure 2-5 shows a model cross section that runs north-south through five legacy wells: [redacted] The nearby proposed Mockingbird INJ No. 01 is shown as well (the blue well path). This cross section depicts the UCZ and other intraformational shale layers (in gray) as well as the [redacted] within the AOR (the red dashed line). Relative offsets of the injection and confining zones across some of the faults are also shown. Figure 2-6 shows the 3D structure framework with the four injector locations.

The target injection zone includes [redacted]. The primary seal is referred to as the UCZ and the secondary seal as the [redacted]. No injection is planned for intervals above the [redacted] reservoir.

[redacted]

2.5.3 Net and Non-Net Model

To guide facies distribution, spectral decomposition of 3D seismic data has been performed, and the resulting three frequency volumes have been used for reservoir environment of deposition (EOD) analysis along with well data and the regional depositional environment references. Figure 2-7 shows an example of interpreted EOD for the [redacted] reservoir. Given the interpreted EODs, a two-step facies modeling approach was adopted to capture the heterogeneity of the reservoirs and seal/intra-shale intervals. The first step was net and non-net modeling that captured the distribution of the net and non-net components of both injection intervals and seal/intra-shale intervals laterally and vertically. The second step was the modeling of different lithofacies (coarse sand, sand, and silty sand) within the net regions defined in the first step.

Within the model boundary, 216 wells contained lithological logs (SP or GR); their locations are presented in Figure 2-8. Figures 2-9 and 2-10 present well cross sections illustrating the stratigraphic and lithologic variation across the AOR. While the confining and injection zone formations are continuous across the AOR, internal variations within each of these zones (e.g., the changing bed thicknesses, intrazonal shales, and lithological variations) were identified in the well logs.

To estimate the Vshale in each well, a shale baseline and a sand baseline—100% values for both—were chosen according to the SP or GR log character of each well and used to calculate the Vshale curve. A “net reservoir” quality rock is defined in well logs where the Vshale is less than 65%.

[redacted]

[redacted]

[redacted]

[redacted]

The interpreted net and non-net logs were upscaled to the geomodel grid and used as hard conditioning data for net/non-net modeling. The upscaled net and non-net data in the model are shown in Figure 2-11. Different modeling approaches have been adopted to capture the heterogeneity in different EODs. A multipoint simulation (MPS) algorithm was used for fluvial channel EOD to capture the curvilinear channel geometry while honoring dense well data. Truncated Gaussian simulation (TGSim) was used for deltaic lobe EOD, and sequential indicator simulation (SISim) was used for coastal plain EOD. These modeling approaches were chosen to adequately capture the geologic heterogeneity while preserving the geologic concept of different EODs. Table 2-1 lists the modeling algorithms and the related parameters.

[redacted]

[redacted]

The MPS algorithm starts with generating 3D training images (TIs), which are conceptual statistical models of the EOD that needs to be simulated. Given a fluvial channel environment, the object-based modeling was determined to be a suitable approach to characterize curvilinear channel geometry and stacking patterns in TI models. Seismic attributes and present-day analogues were leveraged to define the dimensions of these channels. The channel (or net) fraction in the TIs is designed to be close to the reservoir net target fraction that is being simulated. Table 2-2 shows the dimensions used for each of the TIs. Figure 2-12 shows examples of TIs used for different reservoirs.

[redacted]

[redacted]

Once the TIs are ready, the next step is to use them in net and non-net modeling for the fluvial channel EOD, maintaining the target proportions and honoring the upscaled well log. The target proportions of the net and non-net (e.g., shale) for each of the zones were derived using the upscaled well log data and are represented in Table 2-3. Figures 2-13 and 2-14 show the north-south and west-east cross sections, respectively, of the net/non-net facies distributions.

[redacted]

[redacted]

[redacted]

2.5.4 Lithofacies Model

The Vshale log was based mostly on SP, which was the most common lithological log in the data set. In some cases, only GR without SP was available and used for the Vshale log determination. However, these cases made up less than 10% of the total cases modeled. To normalize SP values for upscaling lithologies, the SP log was drift-corrected to force the shale baseline to zero millivolts (mV). In cases of the GR log, the drift correction for the shale baseline (100% shale) was assigned as 150 GAPI units. The Vshale log was then used to determine lithofacies using a cutoff based on the lithology-porosity relationship discussed below.

The injection zone facies classifications are shown in Figure 2-15, where four facies were identified based on the Vshale log. Those classifications are described in Table 2-4.

[redacted]

Table 2-4 – Description of the Facies Classifications

Facies	Volume of Shale (%)
Coarse Sand	<20
Sand	20 to 40
Silty Sand	40 to 65
Shale	>65

The interpreted lithofacies logs were upscaled to model resolution with a bias to the modeled net and not-net intervals. A TGSim algorithm was used to populate the lithofacies distributed within the net region in the 3D model, conditioned to the upscaled lithofacies log data. The statistical parameters and trend maps helped to distribute coarse sand along the core of the net geobodies (e.g., channels, lobes), and sequentially distribute sand and silty sand toward the flank. The variograms for facies modeling are determined based on the geological feature dimensions used in net and non-net modeling along with geological concepts. The values considered for different intervals are shown in Table 2-5.

[redacted]

The net reservoir proportion calculated for each interval was summarized in Table 2-3, and a further breakdown of the facies within the net reservoir is summarized in Table 2-6.

[redacted]

Figures 2-16 and 2-17 present two cross sections across the AOR through different wells, showing modeled lithofacies in the geologic model. The results show excellent correlation between the modeled facies and log assignment. The figures also illustrate the distribution of lithofacies away from the wells. Figure 2-18 presents the map view of representative layers for the [redacted] [redacted] Both net and lithofacies on the figure were mapped based on the interpreted depositional environment for the two injection intervals.

[redacted]

[redacted]

[redacted]

2.5.5 Net-to-Gross Model

The net-to-gross (NTG) model was used to support upscaling from log scale to the 3D geologic model scale. While performing facies upscaling, each geologic model cell is assigned the facies code that has the highest fraction from the respective well log interval. For interbedded reservoirs, the model cells that are assigned to the net facies code may represent a mixture of net/non-net. Figure 2-19 is a well cross section showing several wells with the Vshale log (first column), facies log (second column), upscaled facies log (third column), NTG log (fourth column) and upscaled NTG log (fifth column). The cross section shows that, within the silty intervals (green-colored facies-dominated interval), the upscaled NTG log is not purely zero or 1, but rather some cells have values between zero and 1 due to upscaling.

The NTG property, which represents the proportion of net facies within a grid cell, is introduced to compensate for this upscaling effect. To perform NTG property modeling, first the NTG log is created based on the facies code. For net facies, the NTG value equals 1; for non-net facies, NTG equals zero. Second, the NTG log is upscaled into the geologic model, which recalculates the proportion of net within a grid cell as a fraction between zero and 1.

Third, the NTG histogram is derived per facies. The statistical distribution (histogram) of NTG—derived from the upscaled well logs corresponding to facies—is used as a key model-input parameter, shown in Figure 2-20. With the derived NTG histograms, the NTG property was modeled for four facies using an SGSim algorithm, while conditioned to the upscaled NTG well data. For shale facies in the geomodel grid with NTG greater than zero, it was assumed that the net facies fraction is silty-sand facies. Example cross sections of the NTG model results are shown in Figures 2-21 (north-south) and 2-22 (west-east), which identify the variability of the net thickness between the wells and how the geologic model handled the upscaling.

The NTG property was used to convert the zone gross thickness into net thickness (NTG x Gross_Thickness). Then the zone net-thickness property was used to create the net sand (including coarse sand, sand, and silty sand facies) thickness maps for three of the injection intervals, shown in Figures 2-23 [redacted] and 2-24 [redacted] Also, the net shale (non-net) thickness maps were created from this property to represent the net shale distribution of the [redacted], shown in Figure 2-25.

[redacted]

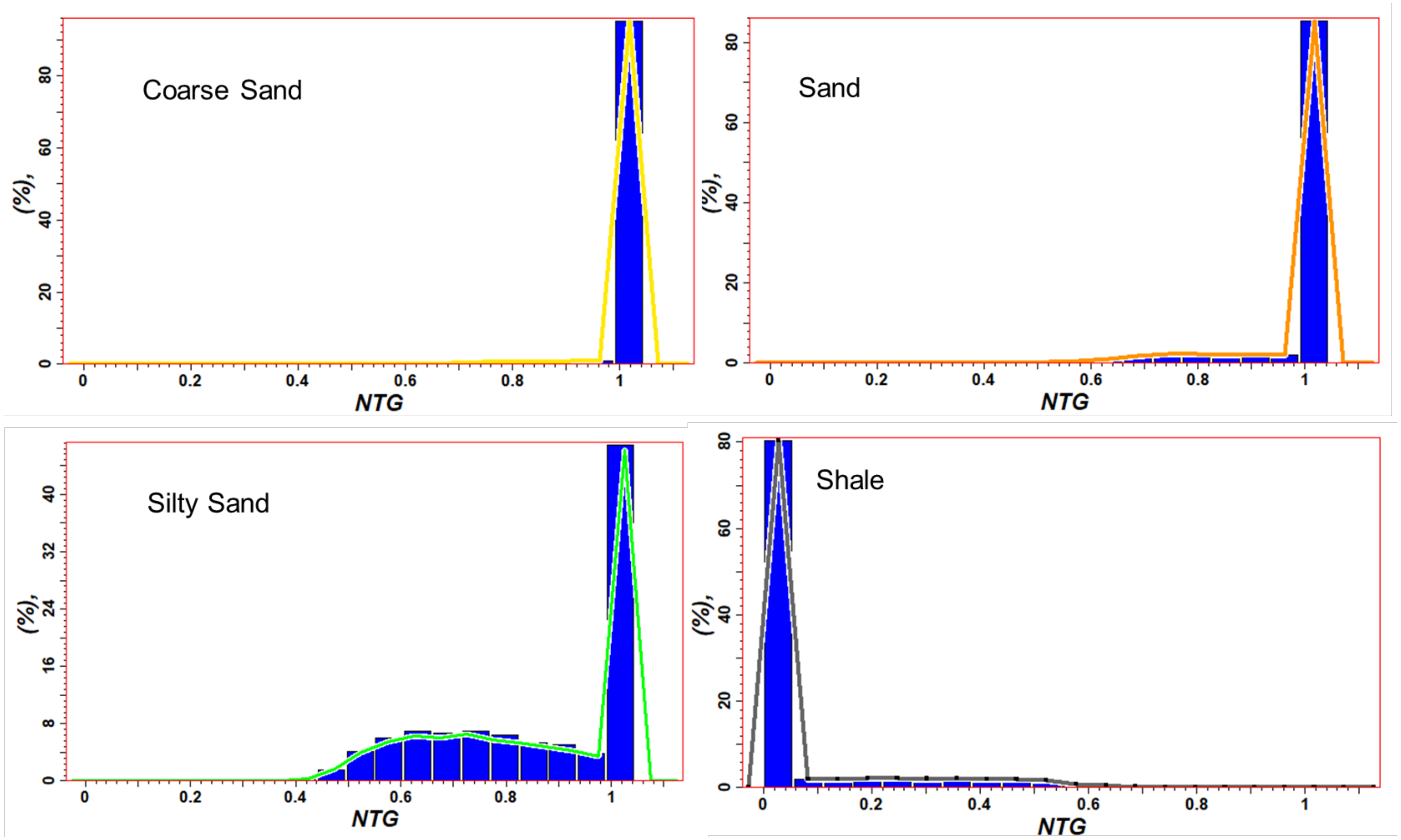

Figure 2-20 – Lithofacies NTG Histograms

[redacted]

[redacted]

[redacted]

[redacted]

[redacted]

2.5.6 Porosity Model

Porosity logs from 20 wells (the green-colored wells in Figure 2-8) within the geologic model boundary were used as hard conditioning data. Compressional sonic data are the most common porosity data source, but some bulk density data also informed porosity estimation. Figure 2-26 shows three wells near the AOR, with the Vshale and the total porosity log calculated for various intervals—including the [redacted]

The estimated average porosity and permeability of the net reservoirs within the [redacted] injection intervals are presented in Table 2-7. [redacted]

[redacted]

The porosity data were de-clustered to remove the sampling bias within the data in the 3D space. These de-clustered data were then used to define the porosity distribution (range) by facies. As part of the modeling process, total porosity logs were then upscaled, with a bias to the modeled facies. Porosity distribution within the injection zone intervals is shown in Figure 2-28 (the bar chart).

The porosity distribution can be further characterized by facies within the [redacted] as shown in Figure 2-28 (the curves). The porosity model is built for each facies using SGSim method, ensuring that the porosity distributions are honored. Finally, this total porosity volume is multiplied with the modeled NTG volume to derive the effective porosity volume for CO2 simulation. Example cross sections of the porosity model results are shown in Figures 2-29 (north-south) and 2-30 (west-east), which show the variability of porosity throughout the model and a decrease in average porosity with depth due to compaction.

[redacted]

[redacted]

[redacted]

[redacted]

[redacted]

2.5.7 Permeability Model

Permeability was modeled based on the porosity-permeability transform functions derived from core collected at a nearby stratigraphic test well [redacted] Separate porosity-permeability transforms were developed for the [redacted]. The nuclear magnetic resonance (NMR) log was calibrated against core and used to define the porosity-permeability function (shown as an NMR-based function in Figures 2-31a and 2-31b) across the range of net reservoir facies. This relationship was then upscaled using Swanson's mean (shown as Swanson's mean original function) to account for differences between core, log, and model scales (Delfiner, 2006). The Swanson's mean relationship was smoothed (shown as Swanson's mean modified function) and then used in the geomodel to generate permeability volumes from modeled porosity volume (Figure 2-31c).

Finally, a scatter using standard Gaussian distribution was added to the permeability volume to mimic the original NMR log-based distribution (Figure 2-31d). Following common geologic modeling practices, [redacted] to remove the uncertainty of the transform function corresponding to higher porosity and permeability values. This permeability volume is multiplied with the modeled NTG volume to derive effective permeability volume.

Example cross sections (north-south and west-east) of the permeability model are shown in Figures 2-32 and 2-33.

[redacted]

[redacted]

[redacted]

2.5.8 Model Uncertainties

The list of uncertainties inherent to the geologic modeling workflow include the following:

- Variation of net thickness between wells in the injection zone, including the continuity of the net facies
- Vertical vs. horizonal permeability relationships adopted based on the log data
- Presence of intrazonal flow barriers, baffles, and pinchouts (permeability architecture)

Based on the available data used in the geologic model, these uncertainties—though present—are not expected to have a significant impact on the model results and delineation of the AOR. The available geologic data are sufficient to characterize the overall depositional system and, in turn, key geologic features in the Mockingbird Project area. Geologic characterization data collected from future drilling activities will be used to further refine the model and reduce these uncertainties.

2.6 Dynamic Model

2.6.1 Model Background

The Petrel-developed geologic model was used as an input into the SLB Intersect numerical reservoir simulator to build the dynamic CO_2 plume and pressure prediction model.

2.6.2 Model Scope and Boundary Conditions

[redacted]

When choosing the simulation model size and the boundary condition, there are two important considerations. First, the simulation model size should be large enough that stabilized CO_2 migration is well within the model boundary. Second, the boundary condition for the simulation model needs to properly reflect areal aquifer connectivity and volume to accurately capture far-field pressure response. As CO_2 is injected, reservoir pressure rises. Depending on the model properties and injection strategy, this pressure perturbation may extend beyond the simulation model boundary. It is not practical to include the full areal extent of pressure perturbations within the simulation. A traditional practice to represent the additional aquifer volume beyond the simulation model boundary is to use pore volume multipliers and transmissibility reduction at the edge of the simulation model.

[redacted] Frio injection intervals at the Mockingbird Project site are characterized as highly connected throughout the region. Therefore, an infinite-acting reservoir boundary condition was selected for the four edges of the rectangular model domain to better simulate the pressure response from CO_2 injection. [redacted] This approach follows common industry practice to represent aquifer volume not explicitly captured in the model domain.

2.6.3 Derivation of Input Parameter Values for Dynamic Modeling

As detailed in this section, ExxonMobil leveraged all available information relevant to the Mockingbird site to derive initial estimates of compressibility, relative permeability, capillary pressure, and reservoir pressure and temperature. Additional data collected through project development activities will be integrated into the site characterization and modeling, as appropriate.

The site-specific characteristics that make the project site ideal for carbon storage are described in *Section 1.11* of *Section 1 – Site Characterization*. In summary, the sands of the [redacted] exhibit high porosity and permeability that are ideal for CO_2 storage and are “of sufficient areal extent, thickness porosity and permeability to receive the total anticipated volume of the carbon dioxide stream” (LAC43: XVII **§3615.A.1**). Both the [redacted] are thick, continuous sealing intervals across the AOR and are sufficient to “contain the injected carbon dioxide stream and displaced formation fluids and allow injection at proposed maximum pressure and volumes without initiating or propagating fractures in the confining zone” (LAC43: XVII **§3615.A.2**).

A summary of input parameter values is provided in Table 2-8.

[redacted]

[redacted]

2.6.3.1 Rock Compressibility

Rock compressibility values leverage information from available literature as well as recent measurements for samples collected at the stratigraphic test well [redacted] in the Gulf Coast region; these samples are from the [redacted] and representative of characteristics expected at the Mockingbird site. Figure 2-34 provides a literature-based relationship between pore volume compressibility and initial porosity. The rock compressibility values measured from core at the stratigraphic test well are shown in Figure 2-35. [redacted]. These values are consistent with the literature-based ranges shown in Figure 2-34.

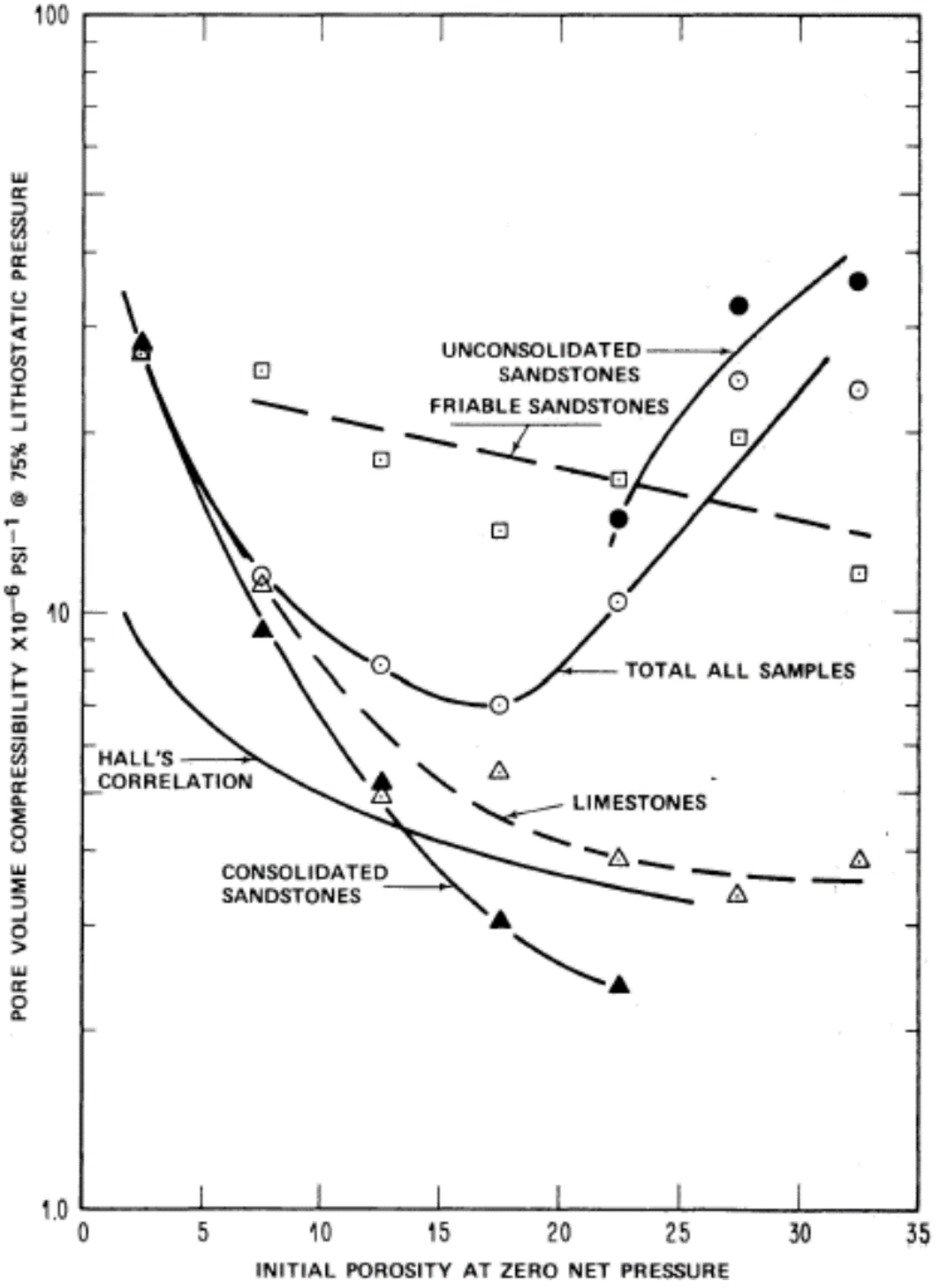

Figure 2-34 – Pore Volume Compressibility as a Function of Initial Porosity (Newman, 1973)

[redacted]

2.6.3.2 Relative Permeability

Relative permeability curves were generated based on research of analogous depositional environments. Traditional core testing has difficulties accurately measuring the end points of the curves, resulting in high irreducible water saturations and low CO_2 endpoints [redacted]. In drainage CO_2-brine relative-permeability experiments, as water saturation decreases, capillary forces become larger (i.e., capillary pressure (P_c)) and increase rapidly in the approach to the irreducible water saturation. During the experiment, the increase in capillary forces limits further reduction in water saturation (i.e., the viscous force is too small relative to the capillary force). This result causes the experimental relative-permeability measurements to end at water saturations higher than the actual irreducible water saturation. [redacted]

[redacted]

[redacted]

The irreducible water saturation was assumed to be in the range of [redacted] based on published values for various sand qualities in the available Gulf Coast regional data. Fitting the end points to the experimental data resulted in brine and CO_2 exponents of [redacted] respectively. The set of relative permeability curves [redacted] is shown in Figure 2-36.

[redacted]

The Corey function for gas and water relative permeability is defined in Equation 1, with the Corey exponents listed in Table 2-9.

$$\text{(Eq. 1)} \qquad k_{rg} = k_{rg,max} \times \left(\frac{S_g - S_{gc}}{1 - S_{gc} - S_{wirr}}\right)^{n_g}$$

$$k_{rw} = k_{rw,max} \times \left(\frac{1 - S_g - S_{wirr}}{1 - S_{wirr}}\right)^{n_w}$$

$$S_{g,max} = 1 - S_{wirr}$$

Gas hysteresis behavior was incorporated into the displacement curves to account for trapped gas as a CO_2 storage mechanism. The approach represents CO_2 replacing water as gas saturation, and the amount of CO_2 increases until it reaches maximum gas saturation. Afterward, during the imbibition process, water drives CO_2 out of the pore space, and gas saturation decreases until it reaches trapped gas saturation (S_{gt}).

2.6.3.3 Capillary Pressure

Capillary pressure functions were formed using the Brooks-Corey capillary pressure model (Equation 2):

(Eq. 2) $$P_c = P_{c,th} \times {S_{wn}}^B$$

$$S_{wn} = \frac{S_w - S_{wirr}}{1 - S_{wirr}}$$

where $P_{c,th}$ is threshold (entry) capillary pressure.

[redacted] was assumed for each permeability bin, which is reasonable for clastic rock at reservoir conditions. The values chosen for each S_{wirr} bin were listed in Table 2-9. In Equation 3, exponent B is related to pore-size distribution index l and estimated based on Burdine's theory:

(Eq. 3) $$B = \frac{1}{I} = -\frac{nw-3}{2}$$

In a gas-water system, the Brooks-Corey capillary pressure model (Eq. 3) indicates that the capillary pressure curves steepen as they approach the irreducible water saturation point. The five sets of capillary curves are plotted in Figure 2-37.

[redacted]

2.6.3.4 Fluid Pressure

A review of the available literature indicates that the [redacted] in this area of the Gulf Coast are expected to have an original reservoir pressure gradient of approximately 0.45 psi per foot (psi/ft) (Kreitler, 1988). The gradient will be updated as needed based on data collected from the stratigraphic test well.

2.6.3.5 Temperature

The local subsurface temperature gradient is estimated to be 1.45°F per 100 feet, based on observations in the offset well Nelda Sue Andrews No. 1 (API No. 1700320432). This estimate is similar to the regional geothermal temperature map published by the Gulf Coast Association of Geological Societies in 2006 (Figure 2-38). This input will be updated as needed based on data collected during drilling of development wells. Mean surface temperature was assumed to be 72°F.

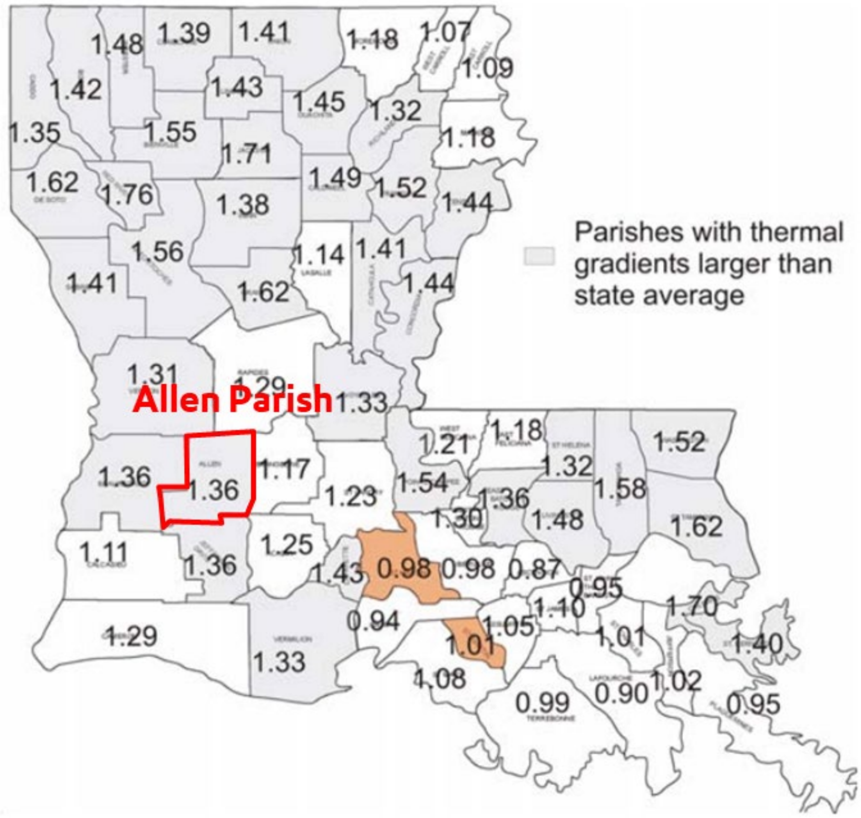

Figure 2-38 – Overall Geothermal Gradient for Louisiana by Parish

2.6.3.6 Initial Saturation

A review of the available literature (Kreitler, 1988) indicates that the target [redacted] in this area of the Gulf Coast are expected to be saline aquifers of 100% water saturation. For the purposes of the simulations, an initial 100% mole fraction of brine was assumed.

2.6.4 Derivation of Input Parameter Values for Fluid Properties

Brine and CO_2 properties (including density, viscosity, and compressibility) are functions of pressure, temperature, and salinity. Industry-standard methods can be employed to determine the pure phase properties and their interaction.

For this model, the CSIW module was used, which—as discussed earlier—can accurately evaluate fluid density and viscosity based on the following:

- The vapor component densities and fugacities are calculated using a cubic EOS.
- The aqueous phase density and viscosity are provided in a solubility table. To generate the tables, the Spycher and Pruess pressure-volume-temperature (PVT) model was used.
- The viscosities are handled using the Lorenz-Bray-Clark model.

2.6.5 Fluid Composition

A regional review of publicly available fluid samples was completed to determine the salinity of the reservoir. Data was taken from the U.S. Geological Survey (USGS) National Produced Waters Geochemical Database, the public online database that stores numerous water samples to help understand regional hydrogeology. Fluid samples taken around the Louisiana southwest parishes, including Allen Parish, were used to identify trends within the injection zone (Szalkowski, 2003). As shown in Figure 2-39, most of the data within the depth range of the project's target injection zone cluster around 100,000 parts per million (ppm). Based on this data, the simulation model was initialized with an average salinity of [redacted]

[redacted]

2.6.5.1 CO_2 Solubility in Brine

Carbon dioxide can dissolve in water and dissolved CO_2 is considered permanently sequestered in the saline aquifer. Therefore, dissolution is an important sequestration mechanism.

[redacted]

[redacted]

[redacted]

Figure 2-40 – CO_2 Solubility in Brine vs. Temperature

2.6.5.2 Brine Solubility in Carbon Dioxide

Brine has a very minor dissolution capacity in CO_2. This behavior is not captured by the Intersect simulation forecasts; however, it has a negligible impact on storage potential.

2.6.5.3 Fluid Density and Viscosity

Carbon dioxide can dissolve in brine, and brine with dissolved CO_2 will have slightly altered density and viscosity. For reference, fluid density and viscosity are provided in Table 2-10 for pure phase CO_2, pure phase brine (without dissolved CO_2) and brine saturated with CO_2, [redacted]

[redacted]

Figure 2-41 illustrates density variation for CO_2 vs. depth. Carbon dioxide becomes denser with increased pressure at deeper intervals, which is partially offset by temperature increases, but generally CO_2 density increases at deeper depths. Figure 2-42 illustrates density variation for brine vs. depth. Brine density decreases at deeper intervals with higher temperature. With CO_2 saturation, brine density increases slightly compared to pure phase.

[redacted]

[redacted]

2.6.5.4 Fluid Compressibility

[redacted]

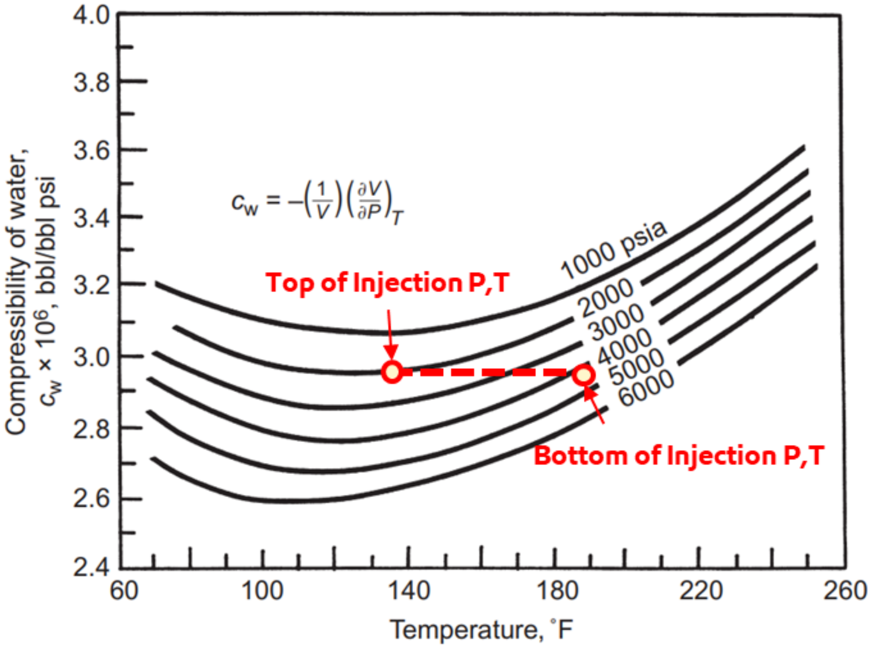

Figure 2-43 – Compressibility of Pure Water as a Function of Temperature and Pressure

[redacted]

2.6.6

2.6.6 Well Operating Parameters

2.6.7

2.6.7.1 Fracture Pressure and Fracture Gradient

Section 1.6 (*Section 1 – Site Characterization*), on geomechanics, details the methodology by which fracture gradients are estimated in each of the injection formations. For reference, the fracture gradients calculated in that section are repeated in Table 2-11.

[redacted]

Using the formation depths consistent with *Section 1*, the maximum allowed bottomhole injection pressures for the injection intervals are shown in Table 2-12, which corresponds to 90% of the estimated fracture pressure.

[redacted]

2.6.7.2 Fluid Injection Rates

The proposed injection wells were simulated using the constraints and input parameters provided in Tables 2-13 through 2-15.

[redacted]

[redacted]

[redacted]

[redacted]

[redacted]

[redacted]

[redacted]

[redacted]

[redacted]

[redacted]

[redacted]

2.7 Model Results

2.7.1 Active Injection Operations of Proposed CO_2 Injector

For each completion interval, the primary control is the target injection rate. In addition, the maximum allowed bottomhole pressure (BHP)—with safety factor—is applied as a constraint, so that if the BHP reaches the constraint, the rate will be reduced so that the constraint is not violated. In the current model, the reservoir quality is sufficient to accommodate the target injection rate without reaching the BHP constraint.

Tables 2-20 through 2-23 summarize the injection rate and pressure parameters for all stages in each injection well, respectively. Bottomhole pressures are reported at mid-sand face in each stage. The depths of these reporting intervals were listed in Tables 2-16 through 2-19.

[redacted]

[redacted]

[redacted]

[redacted]

Continuous injection rates, injection pressures, and associated pressure constraints for each injection well are illustrated in Figures 2-46 through 2-49, respectively. As shown, the operational BHP remains well below the allowed maximum pressure, with at least a 600 psi margin in each zone.

[redacted]

[redacted]

[redacted]

[redacted]

Elevated pressure in the injection intervals quickly dissipates once active injection operations cease. Post-injection, all injection wells are shut in, and the reservoir pressure stabilizes close to initial conditions. Figure 2-50 presents the BHP gradient throughout the life of the project. As shown, the pressure gradient never exceeds the BHP constraint (90% of the fracture gradient) imposed on each well, to allow for the safe injection of supercritical CO_2.

[redacted]

2.7.2 Extent of CO_2 Plume

The areal grid block size in the model was selected to allow for accurate contouring of the plume extent, limit grid distortion effects, and optimize model runtimes. The operational and geologic input parameters described above were used in the Intersect model to generate projections of plume and pressure migration vs. time. Each injection well was initially completed and then recompleted into incrementally shallower portions of the injection intervals per the schedule presented in Figure 2-45.

Figure 2-51 shows the time-dependent, maximum areal extent of the CO_2 plume projected to be present in any of the injection zone layers from the start of operations. The CO_2 saturation and the areal extent of the plumes generated by CO_2 injection expand with time. As the volume of injected CO_2 increases, the CO_2 plumes from each injection well commingle in some of the layers. Once injection stops, the CO_2 footprint migration slows considerably. The combined effects of relative permeability, capillary pressure, CO_2 dissolving in brine, and limited structural dip ultimately arrest the extent of the CO_2 plume migration drift updip to the northwest. Figure 2-52 illustrates the cross-sectional view of the time-dependent CO_2 plume.

[redacted]

[redacted]

As shown in Figure 2-53, the rate of the plume size growth diminishes rapidly following the cessation of injection, [redacted]

[redacted]

2.7.3 Delineation of the Critical Pressure Front

The pressure AOR was delineated by the critical pressure front created by the injection of CO_2 into the injection zone. Critical pressure is the increase in reservoir pressure that has the potential to create a crossflow of brine from the injection zone into the lowermost USDW, assuming the presence of a hypothetical bridging conduit such as an open borehole. The first step to predict the pressure front of interest is to calculate the critical pressure at different depths of the completion intervals. Once critical pressure is estimated, a numerical simulation is used to predict the size and shape of the critical pressure front defined by this pressure contour.

2.7.3.1 Critical Pressure Calculations

[redacted] assumes that the injection reservoir is in hydrostatic equilibrium, neither under- nor overpressured, and that a direct path between the injection zone and lowermost USDW exists. This hypothetical vertical pathway could be an insufficiently plugged and abandoned wellbore or some other subsurface feature.

[redacted] The critical pressure was calculated with input parameters including reservoir depth, USDW depth, wellbore fluid, and reservoir salinity. Injection-interval perforations range in depth [redacted] The total dissolved solids (TDS) of the [redacted] The fluid within the USDW was assumed to be freshwater of 10,000 ppm salinity, with a fluid pressure gradient of [redacted]. For pressure-AOR delineation purposes, the critical pressure threshold is calculated for the full field, then compared with field pressure increase. To illustrate, inputs for an example calculation (evaluated at the top of the [redacted] in Mockingbird INJ No. 01) are provided in Table 2-24.

[redacted]

[redacted]

[redacted]

[redacted]

[redacted]

[redacted]

[redacted]

The critical pressure front, illustrated in Figure 2-54, represents the critical pressure front at the end of each injection stage and maximum pressure front over the complete operating time frame, based on critical pressure calculations detailed in the prior section.

2.7.4 Final AOR

The maximum areal extent of either the CO_2 plume or the critical pressure front, at any given time or depth, was used to define the final AOR boundary. [redacted] The critical pressure front, illustrated in Figure 2-54, represents the maximum areal cone of influence and combines results from the six completion intervals for each of the four injection wells. Superimposing the maximum CO_2 plume and critical pressure boundaries, Figure 2-55 provides the AOR boundary for the project.

[redacted]

[redacted]

2.8 References

Bachu, S. (2012). "Drainage and Imbibition CO2/Brine Relative Permeability Curves at in Situ Conditions for Sandstone Formations in Western Canada." *Energy Procedia*, 37. 10.1016/j.egypro.2013.07.001

Benson, S., Reynolds, R., and Krevor, S. (2013). Relative Permeability Analysis to Describe Multi-Phase Flow in CO2 Storage Reservoirs, No. 2, Global CCS Institute: Melbourne, Australia.

Carlson, D. and McCulloh, R.P. (2006). A Preliminary Examination of Geothermal Gradient Throughout Louisiana's 64 Parishes. The Gulf Coast Association of Geological Societies.

Chen, X., Gao, S., Kianinejad, A., and DiCarlo, D.A. (2017). "Steady-state supercritical CO2 and brine relative permeability in Berea sandstone at different temperature and pressure conditions." *Water Resources Res*. 53, 6312-6321. doi:10. 1002/2017WR020810

Delfiner, P. (2006). Three Statistical Pitfalls of Phi-K Transforms. SPE Annual Technology Conference Exhibition, San Antonio, Texas. September 24-27. SPE-102093.

Djebbar T. and Donaldson, E.C. (2016). Petrophysics - Theory and Practice of Measuring Reservoir Rock and Fluid Transport Properties, 4th edition.

Intersect Technical Description, Reservoir Simulation, Compositional fluid modeling.

Intersect Technical Description, Reservoir Simulation, Component solubility in the aqueous phase.

IPCC (2005). B. Metz, O. Davidson, H. de Coninck, M. Loos, and L. Meyer. Carbon Dioxide Capture and Storage. Cambridge University Press, UK.

Kreitler, C., Akhter, M.S., and Donnelly, A. (1988). Hydraulic-Hydrochemical Characterization of Texas Gulf Coast Saline Formations Used for Deep-Well Injection of Chemical Wastes. Bureau of Economic Geology. University of Texas Austin.

Law, D. and Bachu, S. (1996). Hydrogeological and Numerical Analysis of CO_2 Disposal in Deep Sedimentary Aquifers in the Alberta Sedimentary Basin. Energy Conversion and Management, 37, 1167-1174. https://doi.org/10.1016/0196-8904(95)00315-0

Newman, G.H. (1973). "Pore-volume compressibility of consolidated, friable, and unconsolidated reservoir rocks under hydrostatic loading." *Journal of Petroleum Technology*, 25(02) 129-134. https://doi.org/10.2118/3835-pa

Nicot, J.P., Oldenburg, C., Bryant, S., and Hovorka, S. (2009). Pressure perturbations from geologic carbon sequestration: Area-of-review boundaries and borehole leakage driving forces. C2009 University of Texas. Published by Elsevier Ltd.

Tiab, D. and Donaldson, E. (2016). Petrophysics Theory and Practice of Measuring Reservoir Rock and Fluid Transport Properties, Fourth Edition.

Szalkowski, D. (2003). Low salinity waters in deep sedimentary basins, Louisiana State University and Agricultural and Mechanical College, LSU Scholarly Repository.